Are high-latitude forward-reverse shock pairs driven by CME overexpansion?

W. B. Manchester IV[1] and T. H. Zurbuchen[2]

Received 6 October 2005; revised 20 January 2006; accepted 31 January 2006; published 25 May 2006.

[1] During its passage through the high-latitude heliosphere, Ulysses observed interplanetary coronal mass ejections (ICMEs) bounded by shocks. These forward-reverse shock pairs have only been observed at high latitude in the fast solar wind. It has been suggested (e.g., Gosling et al., 1995) that these shock pairs are the result of expansion of coronal mass ejections into the ambient solar wind, so-called ''overexpansion''. Here we demonstrate an alternative explanation for forward-reverse shock pairs by means of a three-dimensional numerical magnetohydrodynamics (MHD) model of a CME interacting with the solar wind. Our global steady state coronal model possesses fast and slow speed solar wind at high and low latitudes, respectively, reminiscent of near solar minimum conditions. Within this model system, a CME erupts from the coronal streamer belt with an initial speed in excess of 1000 km/s, which naturally drives a forward shock into the ambient solar wind. When the CME is greater than 40 $R_\odot$ from the Sun, we find that a reverse shock forms poleward of the CME as a result of the interaction of the CME with the solar wind. In front of the CME, the slow wind is deflected to higher latitude while behind the CME, fast wind is deflected to low latitude. These deflected streams collide to form a reverse shock. The shock pair formed in this way naturally occurs at high latitude in the fast wind as observed. We will discuss these model results in the context of in situ solar wind data.

Citation: Manchester, W. B., IV, and T. H. Zurbuchen (2006), Are high-latitude forward-reverse shock pairs driven by CME overexpansion?, *J. Geophys. Res.*, *111*, A05101, doi:10.1029/2005JA011461.

1. Introduction

[2] Coronal mass ejections (CMEs) are characterized by large-scale expulsions of 10^{15}–10^{16} g of plasma from the corona into interplanetary space. These eruptions produce significant disturbances in the solar wind that extend far beyond the ejected plasma. For CMEs faster than the ambient solar wind, these disturbances include shock waves driven ahead of the ejecta as they plow through the slower wind. In some instances, such shock waves have purportedly been observed in the low corona as bright loops at the front of CMEs [*Sime and Hundhausen*, 1987; *Raymond et al.*, 2000]. More often CME-driven shocks are observed by spacecraft throughout the heliosphere. Typically, these so-called forward shocks move away from the Sun in the frame of the plasma, and shocked, fast, dense plasma is sunward of the shock front. Examples of the simulated propagation of such shocks to 1 AU can be found, for example in the work of *Wu et al.* [1999], *Riley et al.* [2002], and *Manchester et al.* [2004b]. It is much more rare to observe shocks at 1 AU that are in a reverse configuration. In contrast to a forward shock, a reverse shock moves toward the Sun in the frame of the plasma while actually being carried away from the Sun by the solar wind. In the case of a reverse shock, fast low-density plasma passes through the shock to produce slow dense shocked plasma.

[3] Reverse shocks typically form in conjunction with a forward shock beyond 3 AU and are driven by high-speed solar wind streams [e.g., *Hundhausen and Gosling*, 1976] in corotating interaction regions (CIRs). Forward-reverse shock pairs akin to those associated with CIRs have also been observed on occasion at 1 AU in CME disturbances in the ecliptic [*Gosling et al.*, 1988]. Forward-reverse shock pairs are also observed with CMEs in a configuration in which the forward and reverse shocks lead and trail the ejecta, respectively. In this case the shock pair is believed to be driven by the overexpansion of CMEs with high internal pressure [*Gosling et al.*, 1994a, 1994b; *Reisenfeld et al.*, 2003]. CMEs associated with forward-reverse shock pairs have many distinguishing properties. First, all these CMEs are found at high heliographic latitude embedded in high-speed streams. Furthermore, these CMEs have an expanding velocity profile with a central speed approximately the same as the fast ambient solar wind. These CMEs commonly exhibit roughly symmetric increases in pressure, density, temperature, and magnetic field strength down stream of the shock pairs while the minima of these plasma quantities occur near the centers of the disturbances. The magnetic structures associated with forward-reverse shock pairs often

[1]Center for Space Environment Modeling, University of Michigan, Ann Arbor, Michigan, USA.
[2]Atmospheric, Oceanic, and Space Sciences, University of Michigan, Ann Arbor, Michigan, USA.

0148-0227/06/2005JA011461

resemble magnetic clouds with shock-enhanced field strengths that are typically a factor of 2 or 3 greater than the ambient solar wind field. Counter streaming electrons suggest closed field lines in the CME while the ion charge state of CME plasma is more typical of the ambient solar wind rather than a more highly ionized ejecta. While this is the common and ideal structure of CMEs with forward-reverse shocks, some examples are much more irregular and asymmetric [*Gosling et al.*, 1998]. *Gosling et al.* [1998] have also shown by way of numerical simulations that it is possible to get forward shocks without reverse shocks and reverse shocks without forward shocks from overexpansion, as is observed on occasion.

[4] Here, we examine the high-latitude forward-reverse shock pair produced in a three-dimensional numerical magnetohydrodynamic (MHD) simulation of a flux-rope-driven disturbance propagating to 1 AU through the solar wind. The steady state corona and solar wind of our model are based on *Groth et al.* [2000], which mimics the solar minimum configuration with open magnetic flux extending from the poles and closed flux forming a streamer belt at the equator. The solar wind in this model is bimodal with fast wind at high latitude and slow wind at low latitude as is found in the declining phase of the solar cycle [*Usmanov et al.*, 2000]. Within this system, a Gibson-Low flux rope [*Gibson and Low*, 1998, hereinafter referred to as GL] is placed within the streamer belt with both ends tied to the inner boundary. The placement of a flux rope in the streamer belt follows from the observation that many CMEs originate from coronal streamers [*Hundhausen*, 1987, 1993]. We will show that a reverse shock occurs at high latitude behind the forward shock in such a solar wind because meridional flows induced by the CME tend to interchange the latitudes of the high- and low-latitude streams causing them to collide. This disturbance naturally possesses many features associated with high-latitude CMEs and suggests that high-latitude forward-reverse shock pairs are disturbances that exist poleward of the main ejecta. In this interpretation, overexpansion is not required for the formation of the forward-reverse shock pair.

[5] The simulation presented here is different in several respects relative to previous simulations that have addressed the formation of forward-reverse shocks surrounding CMEs. First, the simulation is three-dimensional, whereas early models were one-dimensional [*Gosling et al.*, 1994a, 1998] and two-dimensional [*Riley et al.*, 1997]. Such three-dimensional simulations allow more realistic modeling of the interaction between CMEs and the heliosphere than one-dimensional or two-dimensional calculations. In this case, the CME is modeled as a magnetic flux rope ejected from the low corona rather than a high-pressure density pulse introduced beyond the magnetosonic point in the solar wind. These features of the CME model are significant to the formation of the reverse shock for two reasons. First, the flux rope is significant in that magnetic tension of the flux rope resists deformation by the bimodal solar wind resulting in a more coherent ejecta in a bimodal flow. The perturbed wind must make its way around a magnetic obstacle that was not present in earlier models. Second, the initiation of the CME in the low corona allows for deflection of the wind close to the Sun that is not possible when the CME is initiated between 20 and 30 $R_\odot$, as has been done in earlier three-dimensional models [*Odstrcil and Pizzo*, 1999a; *Odstrcil and Pizzo*, 1999b]. We will show that the increased deflection of the bimodal wind by the flux rope leads to reverse shock formation without overexpansion and may answer enigmatic questions about the properties of forward-reverse shock pairs associated with CMEs.

[6] It is important to note that the results described here should not strongly depend on the details of the CME initiation model. The exact nature of the initiation process is immaterial to this study, since it exclusively focuses on the CME interaction with the heliosphere. This same simulation is the topic of earlier papers that describe the CME propagation to 1 AU [*Manchester et al.*, 2004b], interaction of a CME-driven forward shock with a bimodal solar wind [*Manchester et al.*, 2005], the evolution of the CME density structure [*Lugaz et al.*, 2005a], and the interaction of multiple CMEs [*Lugaz et al.*, 2005b].

[7] The organization of the paper is as follows. We give a brief description of the conservative form of the equations of MHD and the scheme used to solve them in section 2. Details of the steady state corona and solar wind are given in section 3 along with a brief description of the GL flux rope. Results of the CME simulation are given in section 4, which includes a discussion of formation and propagation of the CME-driven forward-reverse shock pair. Finally, in section 5, we discuss the simulation results and their relevance to observations of forward-reverse shock pairs associated with CMEs.

2. Governing Equations of the MHD Model

[8] In our model of the corona and heliosphere, we assume that the systems are composed of magnetized plasmas that behave as an ideal gas with a polytropic index, $\gamma = 5/3$. The plasma is assumed to have infinite electrical conductivity so that the magnetic field is "frozen" into the plasma. The gravitational force on the plasma is included but only that due to the Sun; there is no self-gravitation of the plasma. Volumetric heating of the plasma of a chosen form is assumed to occur in the corona. With these assumptions, the evolution of the system may be modeled by the ideal MHD equations written in conservative form:

$$\frac{\partial \rho}{\partial t} + \nabla \cdot (\rho u) = 0 \tag{1}$$

$$\frac{\partial (\rho \mathbf{u})}{\partial t} + \nabla \cdot \left[\rho \boldsymbol{u} u + \left(p + \frac{B^2}{8\pi} \right) I - \frac{\boldsymbol{B} B}{4\pi} \right] = \rho \boldsymbol{g} \tag{2}$$

$$\frac{\partial \boldsymbol{B}}{\partial t} + \nabla \cdot (\boldsymbol{u} B - \boldsymbol{B} u) = 0 \tag{3}$$

$$\frac{\partial \varepsilon}{\partial t} + \nabla \cdot \left[\boldsymbol{u} \left(\varepsilon + p + \frac{B^2}{8\pi} \right) - \frac{(\boldsymbol{u} \cdot \boldsymbol{B}) \boldsymbol{B}}{4\pi} \right] = \rho \boldsymbol{g} \cdot \boldsymbol{u} + (\gamma - 1) Q, \tag{4}$$

where ρ is the plasma mass density, $\boldsymbol{u}$ is the plasma velocity, $\boldsymbol{B}$ is the magnetic field, and p is the plasma pressure (sum of the electron and ion pressures). The volumetric heating

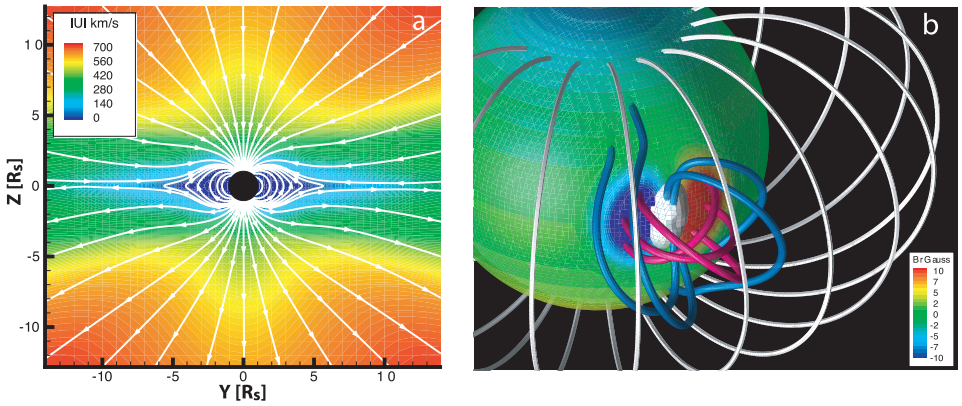

Figure 1. (a) Color image of the velocity magnitude of the steady state solar wind solution in the meridional ($y - z$) plane. "Streamlines" are drawn in white illustrate the direction of the magnetic field in the plane. Note the bimodal nature of the solar wind speed. (b) A three-dimensional representation of the coronal magnetic field at $t = 0$ hours drawn as solid white lines. The flux rope is represented by magenta and blue lines that sample the predominantly toroidal and poloidal magnetic field of the rope, respectively. The white surface is a density isosurface corresponding to 2×10^{-16} g.cm^{-3} and shows the dense core contained in the GL flux rope. The colored sphere shows the magnetic field strength at the base of the model corona.

term, Q, parameterizes the effects of coronal heating as well as heat conduction and radiation transfer (see section 3). The gravitational acceleration is defined as $\boldsymbol{g} = -g(\boldsymbol{r}/r)(R_\odot/r)^2$, where $R_\odot$ is the solar radius and g is the gravitational acceleration at the solar surface. The total energy density, ε, is given by

$$\varepsilon = \frac{\rho u^2}{2} + \frac{p}{\gamma - 1} + \frac{B^2}{8\pi}, \tag{5}$$

where gravity is omitted from the total since it is treated as a momentum source term. This system of equations describes the transport of mass, momentum, and energy with three equations describing the evolution of the magnetic field. These equations are then put in dimensionless form, using values of the density and ion-acoustic wave speed from a suitable part of the physical domain (in this case the low corona) in addition to a reference length scale (in this case the solar radius). The dimensionless equations are then solved, using the block-adaptive tree solar wind Roe-type upwind scheme (BATS-R-US) code [*Powell et al.*, 1999; *Groth et al.*, 2000]. This code is designed to run efficiently on massively parallel computers and solves the equations of MHD with the use of block adaptive mesh refinement (AMR). This feature of the grid allows for orders of magnitude variation in numerical resolution within the computational domain. Such an adaptive grid is necessary to accurately resolve structures such as shocks and current sheets in the context of a global coronal model extending beyond 1 AU.

3. Models of the Steady State Solar Wind and CME

[9] In order to simulate the time-dependent behavior of a CME propagating from the low corona through the solar wind, a representative MHD model of the steady state background solar wind is required. With such a model, the evolution of a CME is then formulated as a propagation problem with the initial condition of the corona and solar wind specified by the steady state solution. In this section we describe our steady state model of the corona and solar wind that is designed to approximately reproduce conditions near solar minimum. The essential features of this model are (see Figure 1a) (1) open magnetic field lines forming coronal holes at high latitude; (2) closed magnetic field lines forming a streamer belt near the Sun at low latitudes; (3) a bimodal solar wind with fast wind over the poles and slow wind at low latitudes. A thin current sheet forms at the tip of the streamer belt and separates opposite directed magnetic flux originating from the two poles. The model is simplified by alignment of the magnetic axis with the z axis so the solution is axisymmetric. Also, solar rotation is included since the domain extends to more than 300 solar radii, at which distance the azimuthal component of the *Parker* [1963] spiral is significant.

[10] The corona is composed of high temperature ($T > 10^6$ K), low mass density ($\rho \approx 10^{-16}$ g cm^{-3}) plasma composed primarily of ionized hydrogen that expands outward at supersonic speeds, and in doing so forms the solar wind [*Parker*, 1963]. The steady state model of the corona and solar wind described here is designed to capture these basic features. The steady state numerical model is made with the assumption that the inner boundary is located at the base of the corona and acts as a reservoir of hot plasma with an embedded magnetic field. The intrinsic magnetic field has dipole and octupole moments aligned with the z axis (there is no quadrupole moment in this model). The maximum field strength at the poles is 8.4 Gauss and 2.2 Gauss at the equator. Volumetric heating of the model corona is introduced to achieve target temperatures of $T_0 = 5.0 \times 10^6$ K near the poles in the coronal hole region, while $T_0 = 2.85 \times 10^6$ K in the streamer belt. Mass density at the base of the corona is uniformly specified at $\rho = 2.5 \times 10^{-16}$ g cm^{-3}. It is important to mention that this heating function was designed to reproduce the observed

fast and slow solar wind and that this temperature structure (hot holes and cool streamer belt) is the opposite of what is measured.

3.1. Computational Mesh

[11] The computational domain for the simulation extends from $-192\ R_\odot < x < 192\ R_\odot$, $-48\ R_\odot < y < 336\ R_\odot$, and $-192\ R_\odot < z < 192\ R_\odot$ with the Sun placed at the origin with the magnetic axis aligned with the z axis. The steady state system is initially resolved with 22,772 self-similar $6 \times 6 \times 6$ blocks containing a total of 4.9 million cells. The blocks are distributed in size over nine levels of refinement with each subsequent level of refinement using cells half the size of the previous level (in each dimension). The cells range in size from $1/32\ R_\odot$ to $8\ R_\odot$ and are spatially positioned to highly resolve the central body and the flux rope as well as the heliospheric current sheet. We then perform two CME simulations in which we resolve the grid at low and then high latitudes along radial lines to 1 AU to form high-resolution corridors along which the CME-driven disturbance travels. At low latitude ($z = 20\ R_\odot$ at 1 AU) we refine the grid to a cell size of $1/8\ R_\odot$, and at high latitude ($z = 120\ R_\odot$ at 1 AU) we refine the grid to $1/2\ R_\odot$. In these two simulations, all things identical except the structure of the numerical mesh.

3.2. Boundary Conditions

[12] We specify appropriate boundary conditions at the inner boundary (the spherical surface $r = R_\odot$) and the outer boundary (the outer surfaces of the rectangular domain) in the following way. Coronal boundary conditions are a function of heliospheric latitude. In the coronal holes the following values are prescribed in ghost cells inside $r = R_\odot$: $\rho = 2.5 \times 10^{-16}$ g cm^{-3}, $p = 5.89 \times 10^{-2}$ dynes cm^{-2}, $\boldsymbol{u} = 0$, and $\boldsymbol{B} = F B_0\}$. These values are then allowed to interact with the solution inside our physical domain through the $r = R_\odot$ boundary by solving the Riemann problem at the boundary. The boundary is treated as a discontinuity in which the inside values are the prescribed boundary values, and the outside values are taken from the adjacent active cell. Solution to the Riemann problem provides the fluxes of mass, energy, momentum, and magnetic field associated with the propagation of waves from the discontinuity. This approach ensures that the appropriate information from the "solar" values is propagated into the solution domain by the numerical flux function used in the scheme. These conditions set up a pressure gradient that drives plasma away from the Sun and permits plasma to pass through the boundary as the mass source for the solar wind. The magnetic field at the surface is specified by the time-independent multipole expansion for the intrinsic field. In the streamer belt the following values are prescribed just inside $r = R_\odot$: $\partial\rho/\partial r = 0$, $\partial p/\partial r = 0$, $\boldsymbol{u} = -\boldsymbol{u}_{outside}$, $\boldsymbol{B} = \boldsymbol{B}_{outside}$, where the subscript *outside* refers to the values just outside $r = R_\odot$, which are computed by the flow solution scheme. These conditions strictly enforce a zero flow at the boundary, both in the radial and tangential directions, with the exception of solar rotational flow. The boundary conditions also enforce continuity of the magnetic field across $r = R_\odot$. This provision allows the magnetic field of the flux rope (prescribed in the streamer belt) to pass through the interface where the footpoints are effectively "line tied" to the rotating surface. At the outer boundary of the domain, the flow is superfast. Thus all waves are exiting the domain, and no information from outside the domain propagates into the domain.

3.3. Steady-State Solar Wind Solution

[13] The solar wind solution is produced by the time evolution of the system subject to the described heating function, intrinsic magnetic field, and boundary conditions. Local time stepping is used to speed up convergence, achieving a near steady state solution after 146,000 iterations with AMR periodically applied to resolve the heliospheric current sheet. Figure 1 depicts the steady state model with a two-dimensional meridional slice on the left and three-dimensional representation on the right. The left panel shows a color image of the velocity magnitude, $|\boldsymbol{u}|$, of the plasma, while the magnetic field is represented by solid white lines. The right panel shows the GL flux rope with magenta and blue lines contained within the streamer belt field shown with white lines. The coronal base is colored to illustrate magnetic field strength. In this model we find that the magnetic field remains closed at low latitude close to the Sun, forming a streamer belt. At high latitude, the magnetic field is carried out with the solar wind to achieve an open configuration. Closer to the equator, closed loops are drawn out and at a distance ($r > 3\ R_\odot$), collapse into a field reversal layer. The resulting field configuration has a neutral line and a current sheet originating at the tip of the streamer belt similar to the numerical solution originally obtained by *Pneuman and Kopp* [1971].

[14] Inspection of Figure 1a reveals a bimodal outflow pattern with slow wind (<400 km/s) leaving the Sun near the equator and high-speed wind (>750 km/s) found above 30° latitude. The variation in solar wind speed in this model results from the variation in latitude of the specified coronal heating and open magnetic flux expansion. The variation in solar wind speed as well as an increase in density near the heliospheric current sheet (the plasma sheet) have been shown to strongly influence the CME-driven forward shock structure [*Odstrcil and Pizzo*, 1999a; *Manchester et al.*, 2005]. Here, we will show that the interaction of the CME with this same wind structure can produce a reverse shock sunward of the CME.

[15] The CME is initiated within this coronal model by superimposing a three-dimensional GL magnetic flux rope in the streamer belt in an initial state of force imbalance as we have previously reported [*Manchester et al.*, 2004a, 2004b, 2005, 2006]. We briefly describe the mathematical form of the GL solutions. The solution for this flux rope is derived by applying a mathematical stretching transformation $r \rightarrow r - a$ to an axisymmetric, spherical ball of twisted magnetic flux in total pressure equilibrium. This mathematical procedure serves two important purposes. First, it generates a geometrically complex solution by distorting the originally spherical, axisymmetric flux rope (centered away from the heliocentric origin) into a teardrop shape with full three-dimensional spatial variation. The second benefit of the stretching transformation is the introduction of Lorentz forces associated with the magnetic field that requires both the pressure and weight of plasma in a $1/r^2$ gravitational field to be in static equilibrium. The density structure of the model possesses a dense helmet streamer

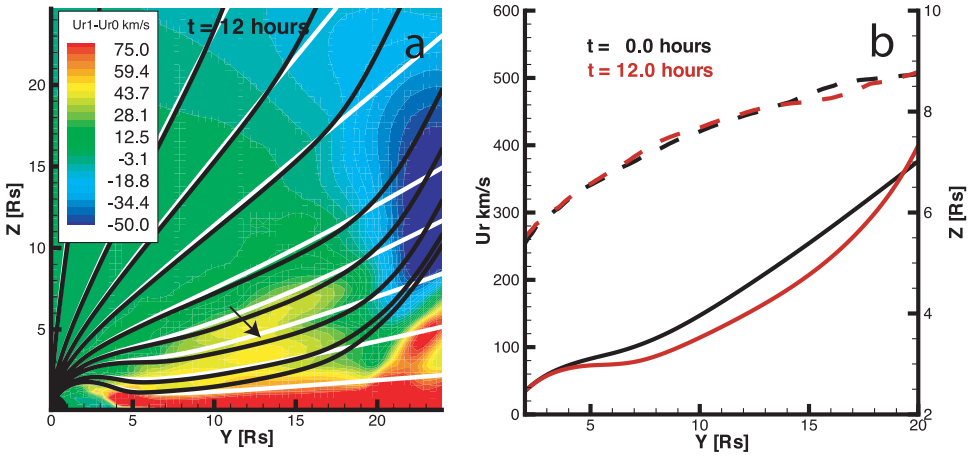

Figure 2. (a) The region directly behind the flux rope shown in the meridional ($y - z$) plane 12 hours after initiation. Two sets of streamlines drawn in white and black illustrate the magnetic field at $t = 0$ and $t = 12$ hours, respectively. The difference of the radial velocity, U_r, to that of the steady state flow is shown in color. Note that the magnetic field and high speed wind are drawn toward the equator in the rarefaction behind the flux rope. (b) The geometry of a single field line is plotted at times $t = 0$ and $t = 12$ hours in solid lines colored black and red, respectively. The radial velocity along the line is plotted with dashed lines colored for the same corresponding times. The plots combine to show that the increase in velocity at midlatitudes is caused by the deflection of high-speed wind to lower latitude rather than the flow being accelerated on the field lines.

containing a cavity embedded with a prominence-type density enhancement. Such long-lived coronal structures are often observed to give rise to CMEs [cf. *Hundhausen*, 1993]. The parameters specifying the magnetic flux rope are found in a series of papers that examined this same model CME. Here, we consider the formation of a reverse shock with the same model.

4. CME Propagation and Shock Formation

[16] In this section we present the results of a numerical simulation designed to study the evolution of a GL flux rope traveling from the corona and propagating to 1 AU. Here, we examine the time evolution of plasma properties at high and low latitude and find very distinct differences between the disturbances found at the two latitudes. Most notably, a forward-reverse shock pair is found at latitudes poleward of the flux rope, while only a single forward shock is found at low latitude. The latitude dependence of the disturbance results from the interaction of the flux rope with the ambient bimodal solar wind. To begin, the CME is initiated at $t = 0.0$ when the flux rope rapidly accelerates to speeds in excess of 1000 km/s and decelerates while driving a fast-mode forward shock. The early evolution of the flux rope is nearly self-similar as the flux over-expands close to the Sun as noted by *Lugaz et al.* [2005a]. This overexpansion however occurs inside the magneto-sonic point and does not drive a reverse shock. Later interaction ($r > 50\ R_\odot$) with the bimodal solar wind distorts the flux rope in two ways. First, far from the Sun the rope ceases to expand radially in the solar wind while continuing to expand laterally with the wind [*Riley and Crooker*, 2004]. Second, the low-latitude portions of the shock and flux rope propagate more slowly than those at high latitude [*Manchester et al.*, 2004b]. These two effects combine to flatten the flux rope and bend it to an outward-concave shape.

[17] The reaction of the CME on the solar wind is not so obvious but has consequences far beyond the immediate proximity of the rope. First, we draw attention to a rarefaction that develops behind the flux rope as it moves out faster than the ambient solar wind. The consequences of this rarefaction are illustrated in Figure 2a, which displays a meridional slice of the region behind the flux rope at $t = 12$ hours. Here, we see two sets of "streamlines", illustrating the magnetic field at $t = 0$ and $t = 12$ hours shown in white and black, respectively. These lines are formed by integrating only the magnetic components that are tangential to the illustrated plane. The difference between the radial velocity, U_r, at times $t = 0$ and $t = 12$ hours is shown in color. Figure 2b, shows the shapes of a field line at times $t = 0$ and $t = 12$ hours plotted as solid black and red lines, respectively. An arrow points to this field line in the figure to the left. The radial velocity on this line is plotted with dashed lines with the same time-color coding. Examining Figures 2a and 2b, we find that equatorward flows develop behind the flux rope that draw the magnetic field and the high speed flow to lower latitudes. The deflection of the fast wind to lower latitude, rather than acceleration of plasma along the field line is clearly responsible for the velocity increase at midlatitude. However, very close to the equator, the flow is accelerated directly by the CME and field lines are deflected to slightly higher latitudes. Overall, the solar wind speed increases behind the flux rope within 45 degrees of the equator.

[18] Next, we look at the large-scale disturbance in the solar wind caused by the passage of the flux rope. In Figures 3a, 3b, and 3c, we present a series of color images that show the radial velocity, U_r, at times $t = 12$, $t = 30$, and

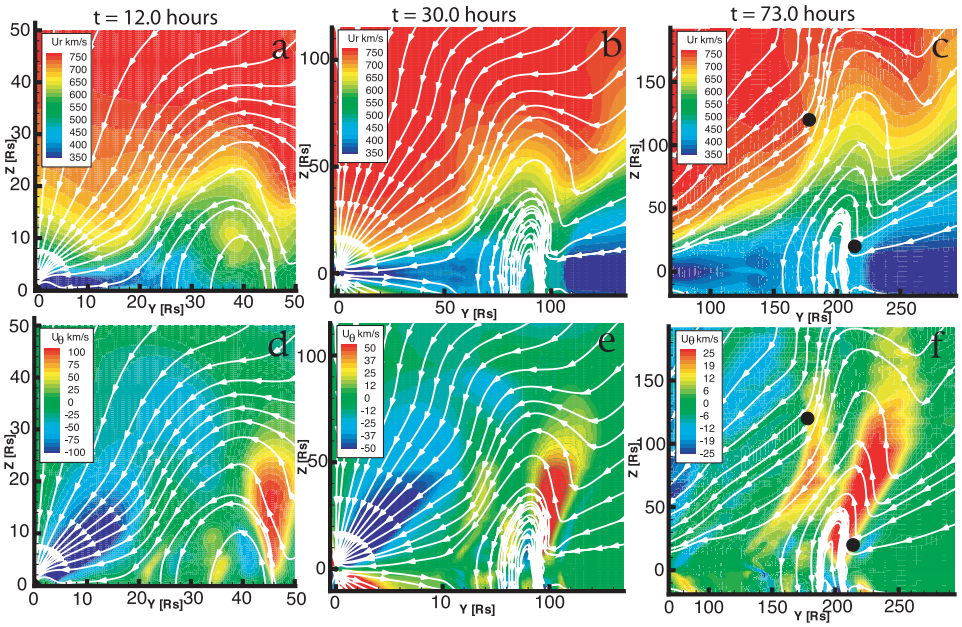

Figure 3. A series of color images that show the radial velocity (above), U_r, at times $t = 12$, $t = 30$, and $t = 73$ hours, respectively, and similarly show the meridional flow, U_θ, at the same times (below). In all panels, the magnetic field is illustrated with white streamlines. Black dots show the locations at 1 AU where time-dependent in situ data is extracted.

$t = 73$ hours, respectively. Figures 3d, 3e, and 3f, similarly show the meridional flow, U_θ, at the same instances. Examining the radial velocity, we find that behind the front shock, a poleward flow around the flux rope deflects the shear layer (separating slow and fast wind) to higher latitude. Figures 3d, 3e, and 3f, more clearly illustrate these meridional deflections. In front of the flux rope, the wind is deflected poleward both at the forward shock and in the sheath. The flow in the sheath is driven by a meridional pressure gradient that drives plasma away from the flux rope. The angular extent of this poleward deflection increases as the CME propagates from the Sun and reaches

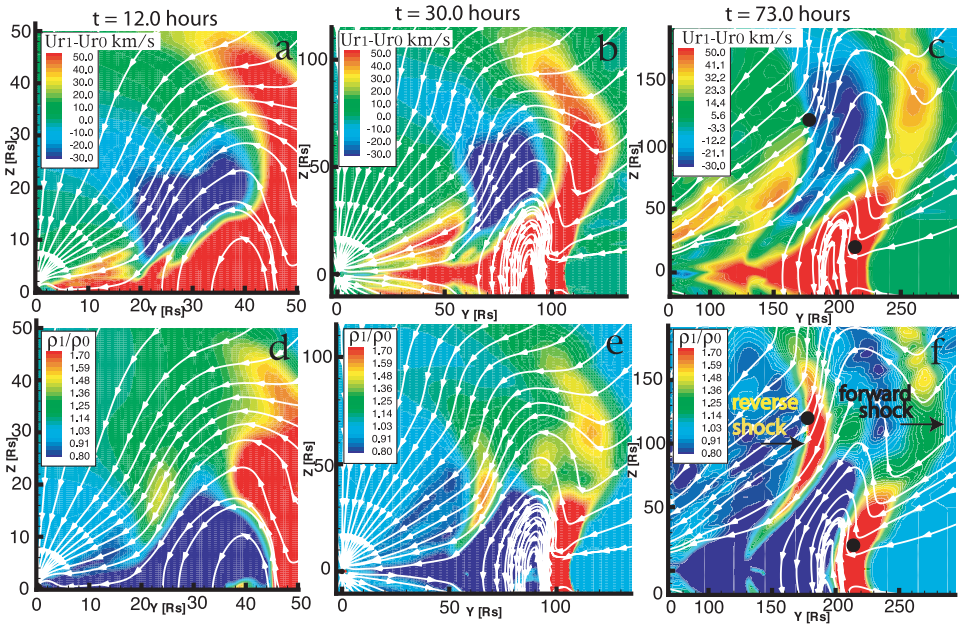

Figure 4. Above, a series of color images that show the radial velocity with the steady state flow subtracted out at times $t = 12$, $t = 30$, and $t = 73$ hours, respectively. Below, the density ratio relative to the initial state at the same times. In all figures, the magnetic field is illustrated with white streamlines.

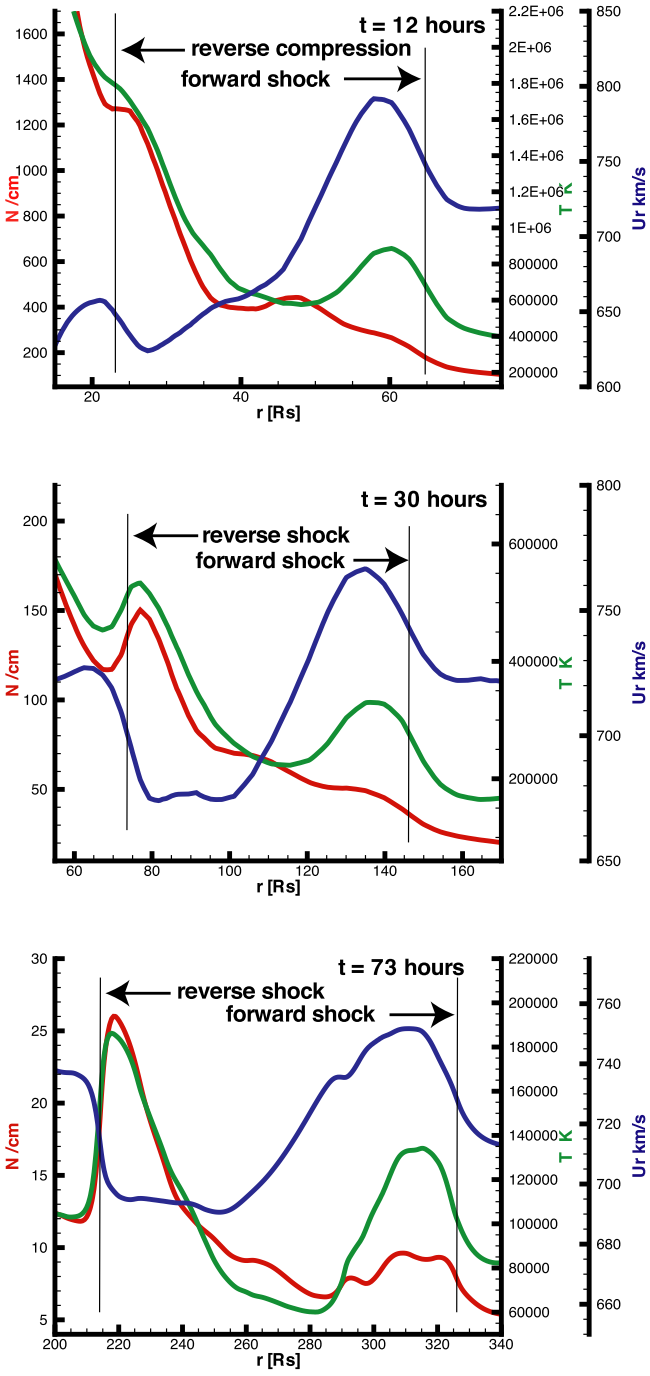

Figure 5. Line plots showing plasma quantities along a radial line at 34.0 degrees latitude centered on the reverse shock. Colored lines show the density (red), temperature (green), and radial velocity (blue) plotted as a function of r at times t = 12, t = 30, t = 73. The shocks appear somewhat smeared out because of the limited numerical resolution.

45 degrees above the equator by t = 73 hours. In Figures 3e and 3f, it can be seen that a poleward deflection also develops behind the flux rope that corresponds with the reverse shock sharply bending the magnetic field. The lateral extent of this poleward flow increases with time, and by t = 73 hours, the flow reaches almost as far as the forward shock seen in Figure 3f. Close to the Sun and prior to the CME, there exists an equatorward flow associated with the super-radial expansion of the open magnetic flux of the solar wind [*Suess et al.*, 1977].

[19] The poleward deflection of the solar wind at the location of a steep meridional gradient in radial velocity causes the fast stream to be radially aligned with a slower moving wind ahead of it over a range of 22–45 degrees latitude. The two streams collide behind the flux rope, first forming a compression well outside of the magnetosonic point at approximately $r = 20\ R_\odot$. The compression steepens into a reverse shock by r = 50 $R_\odot$ and increases in latitudinal extent. By the time the flux rope reaches 1 AU, the reverse shock extends to 45 degrees above the equatorial plane, more than twice the extent of the flux rope. The reverse shock is of the fast-mode variety, which deflects the flow and the magnetic field away from the shock normal. In this case, the reverse shock causes a fast, low-density wind to become a slow, dense wind deflected to go around the magnetic flux rope.

[20] To more clearly illustrate the evolution of the shocks, we show the radial velocity with the ambient flow subtracted out in Figures 4a, 4b, and 4c at times t = 12, t = 30, and t = 73 hours, respectively. The density ratio (current state/initial state) is shown for the same times in Figures 4d, 4e, and 4f. Black dots mark high- and low-latitude locations at 1 AU where the flow will be further examined. Examining the figures, we see that the radial velocity is enhanced behind the forward shock and sunward of the reverse shock by 20–30 km/s. A region of reduced radial velocity is found between the enhancements where the meridional flow has transported slower wind. The density ratio clearly shows a compression behind the top of the flux rope at t = 12 hours that clearly evolves into a shock by t = 30 hours. By t = 73 hours, the compression at the reverse shock is stronger than that of the high-latitude portion of the forward shock.

[21] In Figure 5 we present line plots of plasma quantities along a line that connects the Sun to the high-latitude point (at y = 178 $R_\odot$, z = 120 $R_\odot$, 34.0 degree heliographic latitude shown as a black dot in Figures 3c, 3f, 4c, and 4f). This line passes roughly through the center of the reverse shock, and the sequence of plots at times t = 12, t = 30, t = 73 reveal more closely how the reverse shock evolves. The line plots show the density, temperature, and radial velocity plotted as a function of r with lines colored red, green, and blue, respectively. At time t = 12 hours, a compression develops at r = 20 $R_\odot$, where the density and temperature are elevated, but do not yet increase with radial distance. By t = 30 hours, the compression has steepened into a fast-mode reverse shock located at y = 60 $R_\odot$, where the velocity drops from 728 to 673 km/s. The reverse shock's Mach number increases as the temperature of the solar wind decreases as seen by the larger jumps in the temperature and density at t = 73 hours.

[22] Figure 6 presents a three-dimensional view of the CME 65.2 hours after initiation. The red isosurface shows an increase in density by a factor of 1.3 over the ambient background, while the gray isosurface shows the magnetic flux rope at 25 nT. The equatorial plane is colored to illustrate the velocity magnitude, which shows the forward shock. This forward shock front is clearly visible preceding

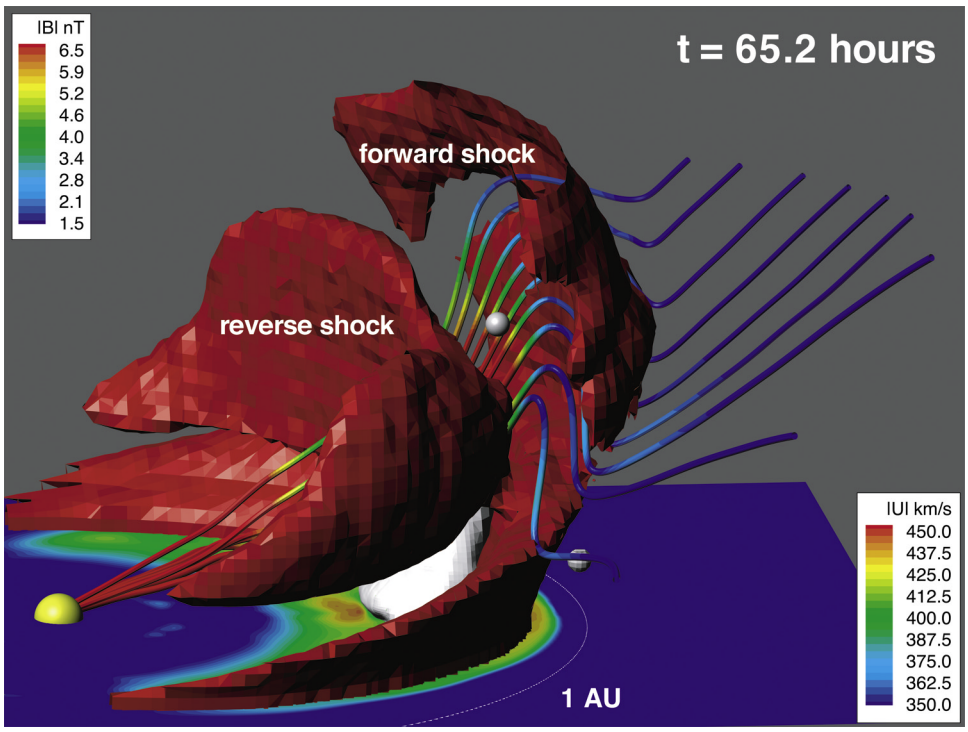

Figure 6. A three-dimensional view of the CME as it appears from 15 degrees above the equatorial plane and 8 degrees from the $-x$ axis, 65.2 hours after initiation. The red isosurface indicates where the density has increased by a factor of 1.3 over the ambient background, clearly showing the forward and reverse shocks. The gray isosurface indicates a magnetic field strength of 25 nT, clearly showing the flux rope in the simulation. Open field lines of the solar wind are colored to illustrate magnetic field strength, and the equatorial plane is colored to illustrate the velocity magnitude. Grey spheres show points at 1 AU that are at heliographic latitudes of 5.4 and 34 degrees.

the flux rope. At low latitude, the shock propagates through the slow dense solar wind at a lower speed than it does through the fast wind found at high latitude. The difference in propagation speed is a consequence of the ambient wind speed and results in an indentation in the shock front that deepens and broadens as the CME travels [*Odstrcil and Pizzo*, 1999a; *Odstrcil and Pizzo*, 1999b; *Manchester et al.*, 2005]. The presence of the reverse shock is manifest in Figure 6 as a density enhancement (part of the red isosurface) sunward of the flux rope. The reverse shock clearly has a large longitudinal extent that reaches almost 180 degrees around the Sun. At high latitude, the fast-mode forward and reverse shocks act to deflect the flow and the magnetic field around the flux rope. Inside of the indentation of the forward shock, the flow is deflected equatorward and then reverses direction behind the shock to move around the flux rope [*Manchester et al.*, 2005]. The manifestation of this reverse shock in Thomson-scattered white light images may be found in the work of *Lugaz et al.* [2005a].

4.1. CME at High and Low Latitudes

[23] We next examine the time evolution of the CME-driven disturbance as it would be observed at high- and low-latitude points (34 degrees and 5.4 degrees, respectively) fixed at 1 AU. The properties of the disturbance as it passes these points are shown in Figure 7. At low latitude, the CME moves sufficiently faster than the slow wind that it leaves a rarefaction in its wake that does not result in a reverse shock. The forward fast-mode shock reaches the low-latitude point in approximately 69 hours, followed by smooth decreases in radial velocity, density, and pressure. The magnetic field strength increases to more than 20 nT upon entering the flux rope then decreases nearly monotonically thereafter. The temperature has a peak at the front and rear boundaries of the flux rope, which is due to numerical dissipation of magnetic flux at the tangential discontinuities between the rope and the solar wind field. These temperature peaks are higher than expected in reality owing to the limited magnetic Reynolds numbers achieved in the simulation. With the exception of the temperature peaks near the flux rope boundaries, the low-latitude signatures are typical of a fast CME plowing through a slow-moving wind ahead.

[24] Next, we look at the disturbance at a latitude of 34 degrees. Here, the forward shock propagates in the fast solar wind and arrives at 1 AU in less than 46 hours followed by a reverse shock at 73 hours. In between the shocks, the radial velocity shows mostly an expanding profile (decreasing speed toward the Sun) with a central speed close to that of the ambient wind. The density, temperature, and total pressure show a roughly symmetric pattern with increases downstream of both forward and reverse shocks and with a relatively flat depression in these quantities near the center of the disturbance. There are significant nonradial deflections to the flow at both high

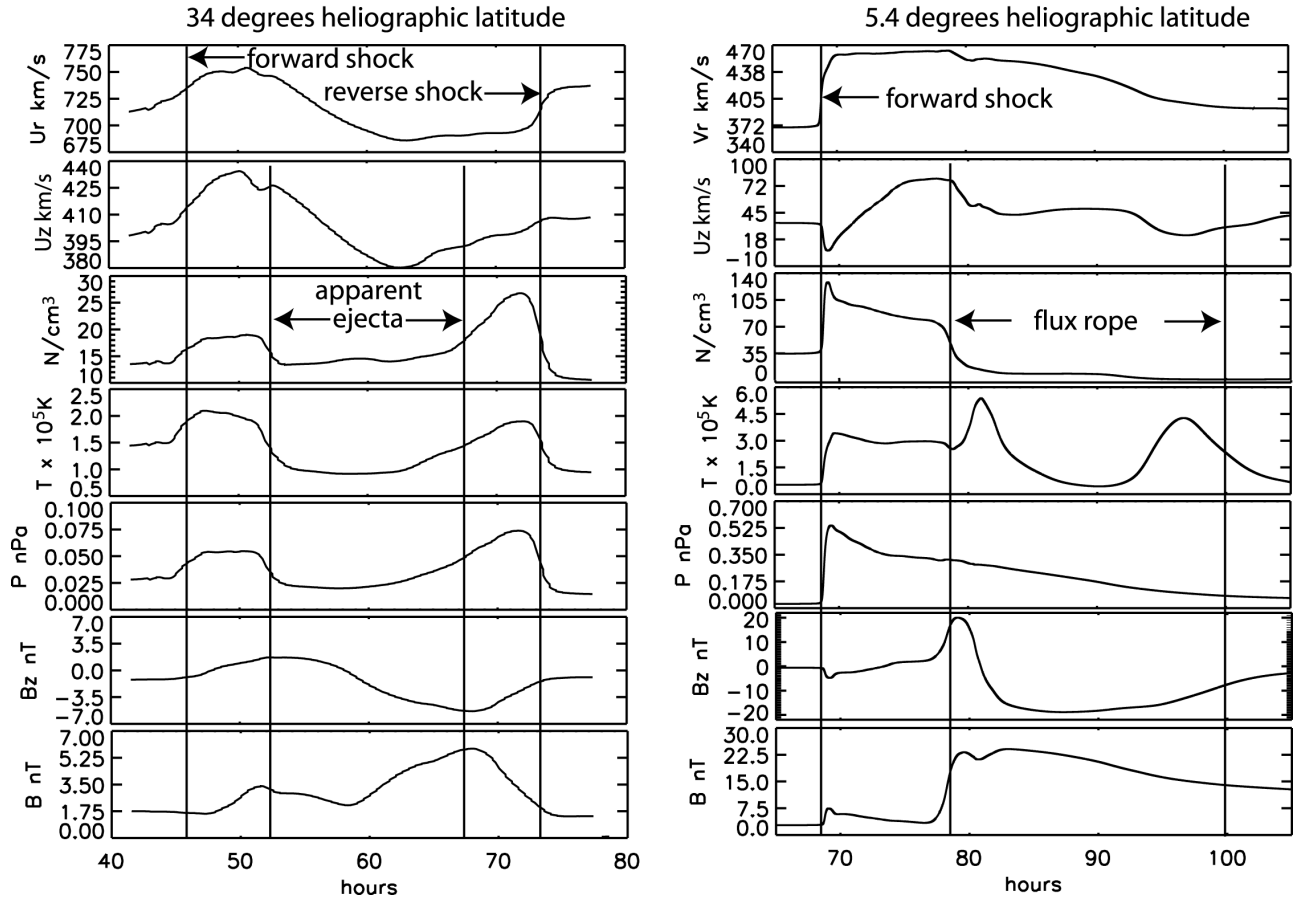

Figure 7. The time evolution of plasma parameters at 1 AU at low latitude (5.4 degrees) in the right column and high latitude (34.0 degrees) in the left column. From top to bottom, the quantities plotted are u_r, u_z, proton number density, n, temperature, T, the total pressure (thermal + magnetic), field component B_z, and the field strength $|\mathbf{F}B|$. At high latitude, the density and radial velocity peak at a single forward shock and then decrease nearly monotonically with time. At high latitude, the radial velocity has an expanding profile (speed decreasing with time), while density and temperature show roughly symmetric peaks behind the forward and reverse shocks.

and low latitudes indicated by U_z. The field strength increases well behind the forward shock where the field lines bend poleward [*Manchester et al.*, 2005]. A similar poleward deflection of the field occurs at the reverse shock. The magnetic field bends behind the two shocks to have a smooth north-south rotation in B_z, and increases in magnitude by a factor of 3. These magnetic signatures could suggest the existence of a flux rope at high latitude well poleward of the actual ejected flux rope.

[25] It is very instructive to examine both high- and low-latitude disturbances produced by a single CME that were observed by Ulysses and IMP8 during February 1994. These data are shown in Figure 8 (as they first appeared in the work of *Gosling et al.* [1995]) and clearly illustrate two distinct disturbances in the solar wind. At this time Ulysses and IMP8 were located 3.53 AU and 1 AU from the Sun, respectively, at latitudes 54 degrees and 7 degrees below the heliographic equator, respectively. This event shows very different signatures at the two locations, with a reverse shock at high latitude but none at low latitude. Near the ecliptic, the disturbance is characterized by a single leading shock at which velocity, density, and magnetic field strength peak in magnitude and then fall off to approach ambient solar wind values. At high latitude, the disturbance contains forward-reverse shocks that are weaker than the single equatorial shock. The density, temperature, and field strength are symmetrically peaked behind the two shocks and decrease toward the center of the disturbance. The velocity at high latitude shows an expanding profile. Our simulation clearly shows many similarities with both the low- and high-latitude observations of this event. In particular, the model is consistent with the high-latitude Ulysses observations of this CME in that both cases have wind speeds 25 km/s faster behind (sunward) the disturbance than ahead of it. In our model, we directly attribute this to the deflection of the high-speed wind to lower latitude behind the CME as shown in Figure 2. Areas where the model shows discrepancies with the data are the field strength at high latitude and the temperature peaks near the flux rope boundaries.

[26] Three magnetic field lines are plotted in Figure 9 at time t = 65.2 hours along with solid lines showing the field strength along these lines in the corresponding color. These open field lines extend far poleward of the flux rope and

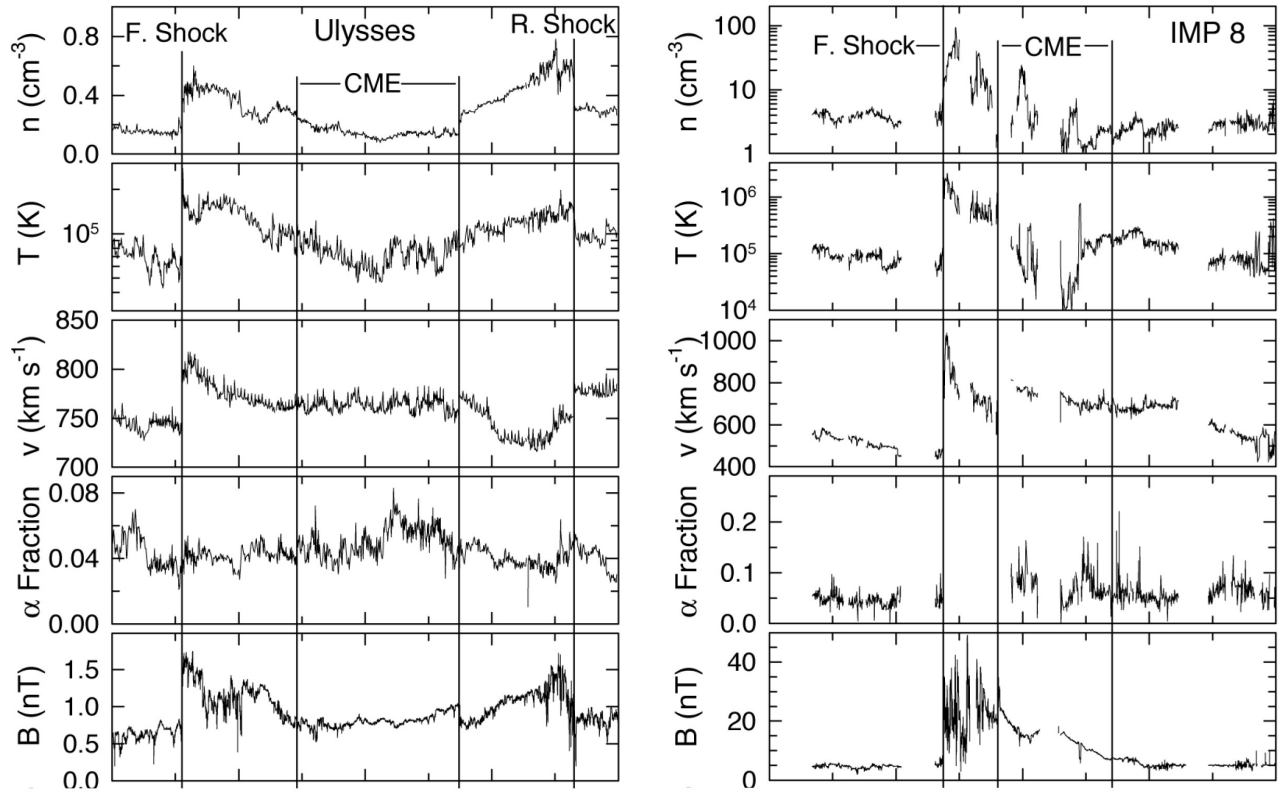

Figure 8. In situ observations made with IMP8 and Ulysses of the low and high-latitude signatures of a CME that left the Sun on 20 February 1994. IMP8 was directly upwind of the Earth while Ulysses was at 3.53 AU and S54.3 degrees when the plasma measurements were made that are shown in the right and left columns, respectively. From top to bottom, plotted as a function of time are the proton number density, proton temperature, velocity magnitude, He^{++}/H^{+} fraction, and magnetic field strength. The data on the left show the the classical signatures of a high-latitude CME with roughly symmetric peaks in density, temperature, and field strength between a forward-reverse shock pair. At low latitude, the density, temperature velocity, and field strength peak at the forward shock and then decrease with time to return to nearly ambient values. (Courtesy of J. T. Gosling, from *Gosling et al.* [1995]).

characterize the high-latitude disturbance caused by the CME. Increases in field strength occur at the forward and reverse shocks as well as behind the forward shock where the field lines bend around the flux rope. There are depressions in the magnetic field strength between the forward and reverse shocks and sunward of the reverse shock that may serve to trap suprathermal electrons. Also, it may be possible that the counterstreaming electrons observed in association with such high-latitude CMEs do not always indicate field lines attached at both ends to the Sun.

[27] It is interesting to compare this simulated disturbance to that of *Riley et al.* [1997], which is two-dimensional and also includes a bimodal solar wind. In that case it was also found that the disturbance extends to high latitude but, unlike our model, the CME ejecta lacks a magnetic field and separates into two distinct pieces because of the solar wind shear. *Riley et al.* [1997] also found meridional flows that transport the slow and fast streams to high and low latitudes, respectively. In their case the physical extent of the deflection is more localized to the shear layer than found here and does not drive a reverse shock. The forward-reverse shock pair found at high latitude in [*Riley et al.*, 1997] is driven by the overexpansion of the CME.

5. Discussion and Conclusions

[28] This simulation addresses observations of so-called overexpanding CMEs reported by *Gosling et al.* [1994a] and subsequent papers [*Gosling et al.*, 1994b, 1995, 1998; *Riley et al.*, 1997; *Reisenfeld et al.*, 2003]. In their interpretation, these CMEs originate in the streamer belt and dynamically propagate into the fast solar wind at high latitude. A forward-reverse shock pair is formed due to high internal pressure of the CME, which causes it to expand into the ambient solar wind. This interpretation may very well hold for some high-latitude CME-driven disturbances, yet there appear to be some puzzles with this explanation. For example, some events have compositional signatures indistinguishable from the coronal hole associated wind. Second, it is not obvious from the overexpanding CME model why the reverse shock forms outside the magnetosonic point, which is necessary for it to travel out with the solar wind [*Gosling et al.*, 1994b]. Third, there

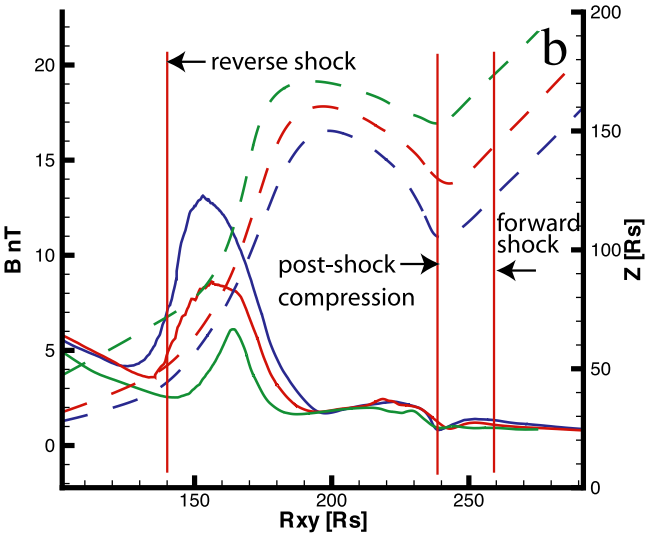

Figure 9. The shape of three high-latitude magnetic field lines plotted as dashed lines and the field strength on those lines plotted in the corresponding color at time t = 65.2 hours. Increases in field strength occur at the forward and reverse shocks as well as in the sheath (postshock compression) where the field lines bend around the flux rope. Here $R_{xy} = \sqrt{x^2 + y^2}$.

have not been any observations of overexpanding CMEs in the ecliptic even though there are plenty of CMEs there that occur in conjunction with coronal hole boundaries [*Hundhausen*, 1993].

[29] Our model offers a different explanation of these events relying on the three-dimensional interaction of a CME with the structured solar wind. The forward-reverse shock pair is a natural consequence of this interaction, which results from large-scale meridional deflections of the solar wind. This explanation naturally addresses some shortcomings of the overexpansion model. The events often have compositional signatures of coronal holes suggesting that they are composed of coronal-hole associated fast streams. The forward-reverse shock pair in our model forms as a result of the solar wind deflection by the CME and therefore does not originate from within the magnetosonic point where the reverse shock would be lost. Also, our mechanism is clearly a high-latitude effect that relies on the overall heliospheric structure modeled here. It is therefore not expected that the same should happen at low latitudes. Our model's dependence on global solar wind structure also explains why CMEs with forward-reverse shock pairs are not found during solar maximum when the solar wind is highly structured and largely lacking a fast component [*Reisenfeld et al.*, 2003]. Finally, it is worth reiterating how important multidimensional interactions are for the propagation and identification of CMEs. These interactions affect the heliosphere well beyond the actual ejecta and have important consequences for the heliospheric structure on a larger scale.

[30] Still, there are features of high-latitude forward-reverse shock pairs that our model does not yet readily explain. Most notably, occurrences of bidirectional electrons often seem to suggest the presence of closed field lines in high-latitude disturbances [*Gosling et al.*, 1994a], which are difficult to account for on open field lines. *Gosling et al.* [2001] have recently pointed out that there may be important previously unrecognized challenges in interpreting bidirectional electron data. These particles are intrinsically nonlocal and therefore difficult to interpret. Also, some high-latitude events do have He^{++}/H signatures of CMEs. This study, however, suggests the utility of compositional measurements for the in situ identification of CMEs. *Richardson and Cane* [2004] and *Zurbuchen et al.* [2003] have pointed out that these compositional signatures are reliable for identifying approximately 85 percent of CMEs. Finally, it should be noted that in situ data have not yet yielded systematic signatures of meridional flows associated with forward-reverse shock pairs that are like those found in our model.

[31] **Acknowledgments.** The authors would like to thank Jack Gosling for discussion and comments concerning this manuscript as well as for providing Figure 8. The simulation reported here was carried out on an Origin3800 supercomputer at NASA Ames. Ward Manchester was supported by Department of Defense MURI grant F49620-01-1-0359, NSF CISE grant ACI-9876943, NSF ITR grant 0325332, and NASA AISRP grant NAG5-9406 at the University of Michigan. W.M. was also supported by LWS grant LWS03-0130-0149 in a subcontract from JPL.

[32] Shadia Rifai Habbal thanks Sarah Gibson and John T. Gosling for their assistance in evaluating this paper.

References

Gibson, S., and B. C. Low (1998), A time-dependent three-dimensional magnetohydrodynamic model of the coronal mass ejection, *Astrophys. J.*, *493*, 460–473.

Gosling, J. T., S. J. Bame, E. J. Smith, and M. E. Burton (1988), Forward-reverse shock pairs associated with transient disturbances in the solar wind at 1 AU, *J. Geophys. Res.*, *93*, 8741–8748.

Gosling, J. T., S. J. Bame, D. J. McComas, J. L. Phillips, E. E. Scime, V. J. Pizzo, B. E. Goldstein, and A. Balogh (1994a), A forward-reverse shock pair in the solar wind driven by over-expansion of a coronal mass ejection: Ulysses observations, *Geophys. Res. Lett.*, *21*, 237–240.

Gosling, J. T., D. J. McComas, J. L. Phillips, A. Weiss, V. J. Pizzo, B. E. Goldstein, and R. J. Forsyth (1994b), A new class of forward-reverse shock pairs in the solar wind, *Geophys. Res. Lett.*, *21*, 2271–2274.

Gosling, J. T., D. J. McComas, J. L. Phillips, V. J. Pizzo, B. E. Goldstein, R. J. Forsyth, and R. P. Lepping (1995), A CME-driven solar wind disturbance observed at both low and high heliographic latitudes, *Geophys. Res. Lett.*, *22*, 1753–1756.

Gosling, J. T., P. Riley, D. J. McComas, and V. J. Pizzo (1998), Over-expanding coronal mass ejections at high heliographic latitudes: Observations and simulations, *J. Geophys. Res.*, *103*, 1941–1954.

Gosling, J. T., R. M. Skoug, and W. C. Feldman (2001), Solar wind electron halo depletions at 90 degree pitch angle, *Geophys. Res. Lett.*, *28*, 4155.

Groth, C. P. T., D. L. DeZeeuw, T. I. Gombosi, and K. G. Powell (2000), Global three-dimensional MHD simulation of a space weather event: CME formation, interplanetary propagation, and interaction with the magnetosphere, *J. Geophys. Res.*, *105*, 25,053–25,078.

Hundhausen, A. J. (1987), The origin and propagation of coronal mass ejections, *Solar Wind Six*, edited by V. J. Pizzo, T. E. Holzer and D. G. Sime, *Tech. Note NCAR/TN-306+Proc*, pp. 181-214, Natl. Cent. for Atmos. Res., Boulder, Colo.

Hundhausen, A. J. (1993), Sizes and locations of coronal mass ejections: SMM observations from 1980 and 1984–1989, *J. Geophys Res.*, *98*, 13,177–13,200.

Hundhausen, A. J., and J. T. Gosling (1976), Solar wind structure at large heliocentric distances: An interpretation of Pioneer 10 observations, *J. Geophys Res.*, *81*, 1436–1440.

Lugaz, N., W. B. Manchester IV, and T. I. Gombosi (2005), The evolution of coronal mass ejection density structures, *Astrophys. J.*, *627*, 1019–1030.

Lugaz, N., W. B. Manchester IV, and T. I. Gombosi (2005), Numerical simulation of the interaction of two coronal mass ejections from Sun to Earth, Ejection Density Structures, *Astrophys. J.*, *634*, 651–662.

Manchester, W. B., IV, T. I. Gombosi, I. Roussev, D. L. DeZeeuw, I. V. Sokolov, K. G. Powell, G. Tóth, and M. Opher (2004a), Three-

dimensional MHD simulation of a flux rope driven CME, *J. Geophys. Res.*, *109*, A01102, doi:10.1029/2002JA009672.

Manchester, W. B., IV, T. I. Gombosi, I. Roussev, A. J. Ridley, D. L. DeZeeuw, I. V. Sokolov, K. G. Powell, and G. Tóth (2004b), Modeling a space weather event from the Sun to The Earth: CME generation and interplanetary propagation, *J. Geophys. Res.*, *109*, A02107, doi:10.1029/2003JA010150.

Manchester, W. B., IV, T. I. Gombosi, D. L. DeZeeuw, I. V. Sokolov, I. Roussev, K. G. Powell, J. Kota, G. Tóth, and T. H. Zurbuchen (2005), Coronal mass ejection shock and sheath structures relevant to particle acceleration, *Astrophys. J.*, *622*, 1225–1239.

Manchester, W. B., IV, A. J. Ridley, T. I. Gombosi, and D. L. DeZeeuw (2006), Modeling the Sun-to-Earth propagation of a very fast CME, *Adv. Space Res.*, in press.

Odstrcil, D., and V. J. Pizzo (1999a), Three-dimensional propagation of coronal mass ejections (CMEs) in a structured solar wind flow: 1. CME launched within the streamer belt, *J. Geophys. Res.*, *104*, 483–492.

Odstrcil, D., and V. J. Pizzo (1999b), Three-dimensional propagation of coronal mass ejections (CMEs) in a structured solar wind flow: 2. CME launched adjacent to the streamer belt, *J. Geophys. Res.*, *104*, 493–503.

Parker, E. N. (1963), *Interplanetary Dynamical Processes*, Wiley-Interscience, Hoboken, N. J.

Pneuman, G. W., and R. A. Kopp (1971), Gas-magnetic field interactions in the solar corona, *Sol. Phys.*, *18*, 258–270.

Powell, K. G., P. L. Roe, T. J. Linde, T. I. Gombosi, and D. L. DeZeeuw (1999), A solution-adaptive upwind scheme for ideal magnetohydrodynamics, *J. Comput. Phys.*, *154*, 284.

Raymond, J. C., B. J. Thompson, O. C. St. Cyr, N. Gopalswamy, S. Kahler, M. Kaiser, A. Lara, A. Ciaravella, M. Romoli, and R. ONeal (2000), SOHO and radio observations of a CME shock wave, *Geophys. Res. Lett.*, *27*, 1439–1442.

Reisenfeld, D. B., J. T. Gosling, R. J. Forsyth, P. Riley, and O. C. St. Cyr (2003), Properties of high-latitude CME-driven disturbances during Ulysses second northern polar passage, *Geophys. Res. Lett.*, *30*(19), 8031, doi:10.1029/2003GL017155.

Richardson, I. G., and H. V. Cane (2004), Identification of interplanetary coronal mass ejections at 1 AU using multiple solar wind plasma composition anomalies, *J. Geophys. Res.*, 109, A09104, doi:10.1029/2004JA010598.

Riley, P., and N. U. Crooker (2004), Kinematic treatment of coronal mass ejection evolution in the solar wind, *Astrophys. J.*, *600*, 1035–1042.

Riley, P., J. T. Gosling, and V. J. Pizzo (1997), A two-dimensional simulation of the radial and latitudinal evolution of a solar wind disturbance driven by a fast, high-pressure coronal mass ejection, *J. Geophys. Res.*, *102*, 14,677–14,685.

Riley, P., J. A. Linker, Z. Mikić, D. Odstrcil, V. J. Pizzo, and D. F. Webb (2002), Evidence of posteruption reconnection associated with coronal mass ejections in the solar wind, *Astrophys. J.*, *578*, 972–978.

Sime, D. G., and A. J. Hundhausen (1987), The coronal mass ejection of July 6, 1980: A candidate for interpretation as a coronal shock wave, *J. Geophys Res.*, *92*, 1049–1055.

Suess, S. T., A. K. Richter, C. R. Winge, and S. F. Nerney (1977), Solar polar coronal hole: A mathematical simulation, *Astrophys. J.*, *217*, 296–305.

Usmanov, A. V., M. L. Goldstein, B. P. Besser, and J. M. Fritzer (2000), A global MHD solar wind model with WKB Alfvén waves: Comparison with Ulysses data, *J. Geophys. Res.*, *105*, 12,675–12,696.

Wu, S. T., W. P. Guo, D. J. Michels, and L. F. Burlaga (1999), MHD description of the dynamical relationships between a flux rope, streamer, coronal mass ejection, and magnetic cloud: An analysis of the January 1997 sun-earth connection event, *J. Geophys. Res.*, *104*, 14,789–14,801.

Zurbuchen, Z. H., L. A. Fisk, S. T. Lepri, and R. von Steiger (2003), The composition of interplanetary coronal mass ejections, in *Solar Wind Ten*, edited by M. Velli, R. Bruno, and F. Malara, *AIP Conf. Proc.*, *679*, 604–607.

W. B. Manchester IV, Center for Space Environment Modeling, University of Michigan, 2455 Hayward Street, Ann Arbor, MI 48109, USA. (chipm@umich.edu)

T. H. Zurbuchen, Atmospheric, Oceanic, and Space Sciences, University of Michigan, 2455 Hayward Street, Ann Arbor, MI 48109, USA.